

## Characterization of Lipid-Templated Silica and Hybrid Thin Film Mesophases by Grazing Incidence Small-Angle X-ray Scattering

Darren R. Dunphy,<sup>†</sup> Todd M. Alam,<sup>‡</sup> Michael P. Tate,<sup>§,○</sup> Hugh W. Hillhouse,<sup>§</sup> Bernd Smarsly,<sup>||</sup> Andrew D. Collord,<sup>‡</sup> Eric Carnes,<sup>†</sup> Helen K. Baca,<sup>†</sup> Ralf Köhn,<sup>†,⊥</sup> Michael Sprung,<sup>#,♦</sup> Jin Wang,<sup>#,</sup> and C. Jeffrey Brinker<sup>\*,†,▽</sup>

<sup>†</sup>University of New Mexico/NSF Center for Micro-Engineered Materials, Department of Chemical and Nuclear Engineering, Albuquerque, New Mexico 87131, <sup>‡</sup>Department of Electronic and Nanostructured Materials, Sandia National Laboratories, Albuquerque, New Mexico 87185, <sup>§</sup>School of Chemical Engineering, Purdue University, 480 Stadium Mall Drive, West Lafayette, Indiana 47907, <sup>||</sup>Physikalisch-Chemisches Institut, Justus-Liebig-University Giessen, Heinrich-Buff-Ring 58, D-35392 Giessen, Germany, <sup>⊥</sup>Department of Chemistry & Biochemistry, University of Munich, Butenandtstr. 5-13 (E), 81377 Munich, Germany, <sup>#</sup>Advanced Photon Source, Argonne National Laboratory, 9700 S Cass Avenue, Argonne, Illinois 60439, and <sup>▽</sup>Advanced Materials Laboratory, Sandia National Laboratories, Albuquerque, New Mexico 87185. <sup>○</sup>Present address: Dow Chemical Company, Midland, Michigan 48674. <sup>♦</sup>Present address: HASYLAB at DESY, D-22607 Hamburg, Germany.

Received March 2, 2009. Revised Manuscript Received April 24, 2009

The nanostructure of silica and hybrid thin film mesophases templated by phospholipids via an evaporation-induced self-assembly (EISA) process was investigated by grazing-incidence small-angle X-ray scattering (GISAXS). Diacyl phosphatidylcholines with two tails of 6 or 8 carbons were found to template 2D hexagonal mesophases, with the removal of lipid from these lipid/silica films by thermal or UV/O<sub>3</sub> processing resulting in a complete collapse of the pore volume. Monoacyl phosphatidylcholines with single tails of 10–14 carbons formed 3D micellar mesophases; the lipid was found to be extractable from these 3D materials, yielding a porous material. In contrast to pure lipid/silica thin film mesophases, films formed from the hybrid bridged silsesquioxane precursor bis(triethoxysilyl)ethane exhibited greater stability toward (both diacyl and monoacyl) lipid removal. Ellipsometric, FTIR, and NMR studies show that the presence of phospholipid suppresses siloxane network formation, while actually promoting condensation reactions in the hybrid material. 1D X-ray scattering and FTIR data were found to be consistent with strong interactions between lipid headgroups and the silica framework.

### Introduction

Evaporation-induced self-assembly (EISA),<sup>1,2</sup> employing amphiphilic surfactants or block copolymers as structure directing agents (SDAs), has been proven to be a versatile route for the synthesis of ordered thin film mesophases characterized by a narrow pore size distribution and a well-defined pore network structure. In this process, a homogeneous alcohol/water solution of a soluble silica precursor, acid catalyst, and surfactant (present at a concentration much less than where bulk mesophases appear) undergoes preferential evaporation of alcohol and then water during film deposition, thus increasing the concentration of silica and surfactants and driving the self-assembly of ordered surfactant/silica mesophases.<sup>1</sup> Subsequent removal of the surfactant template by pyrolysis, UV exposure,<sup>3</sup> or solvent extraction leaves a porous silica fossil of the original mesophase. The pore size of these materials, along with the mesophase identity, can be tuned through the size and shape of the surfactant (as understood by the critical packing parameter model)<sup>4</sup> as well as control of

parameters such as the surfactant/silica and water/silica molar ratios. Common mesophases formed by EISA include lamellar, 2D hexagonal, and various 3D structures including cubic and 3D hexagonal phases.<sup>2</sup> Importantly, the silica precursor can be replaced with other soluble hydrophilic precursors to form non-silica metal oxide frameworks (TiO<sub>2</sub>, SnO<sub>2</sub>, etc.)<sup>2,5,6</sup> as well as with precursors containing carbon–silicon bonds, producing hybrid functional materials.<sup>2,7</sup> Numerous applications have been proposed for these materials, including separation membranes,<sup>8</sup> sensors,<sup>9</sup> and low-*k* dielectrics.<sup>10</sup>

Despite over a decade of research on surfactant-directed synthesis of porous or composite materials, one class of amphiphilic SDA that has not been investigated in any great detail is phospholipids. Phospholipids are known as components of cell membranes and liposomes, but their use to direct inorganic mesophases is largely unexplored. Recently, we demonstrated

\*To whom correspondence should be addressed. E-mail: cjbrink@sandia.gov.

(1) Lu, Y. F.; Ganguli, R.; Drewien, C. A.; Anderson, M. T.; Brinker, C. J.; Gong, W. L.; Guo, Y. X.; Soye, H.; Dunn, B.; Huang, M. H.; Zink, J. I. *Nature* **1997**, *389*, 364–368.

(2) Sanchez, C.; Boissiere, C.; Grosso, D.; Laberty, C.; Nicole, L. *Chem. Mater.* **2008**, *20*, 682–737.

(3) Clark, T.; Ruiz, R. D.; Fan, H.; Brinker, C. J.; Swanson, B. I.; Parikh, A. N. *Chem. Mater.* **2000**, *12*, 3879–3884.

(4) Israelachvili, J. N. *Intermolecular and Surface Forces*, 2nd ed.; Academic Press: New York, 1991.

(5) Alberius, P. C. A.; Frindell, K. L.; Hayward, R. C.; Kramer, E. J.; Stucky, G. D.; Chmelka, B. F. *Chem. Mater.* **2002**, *14*, 3284–3294.

(6) (a) Crepaldi, E. L.; Soler-Illia, G. J. D. A.; Bouchara, A.; Grosso, D.; Durand, D.; Sanchez, C. *Angew. Chem., Int. Ed.* **2003**, *42*, 347–351. (b) Urade, V.; Hillhouse, H. W. *J. Phys. Chem. B* **2005**, *109*, 10538–10541.

(7) Dunphy, D. R.; Smarsly, B.; Brinker, C. J. In *The Supramolecular Chemistry of Organic-Inorganic Hybrid Materials*; Rurack, K., Ed.; John Wiley & Sons, Inc.: Hoboken, NJ, in press.

(8) Jiang, Y.-B.; Xomertakis, G.; Chen, Z.; Dunphy, D.; Kissel, D. J.; Cecchi, J. L.; Brinker, C. J. *J. Am. Chem. Soc.* **2007**, *129*, 15446–15447.

(9) Innocenzi, P.; Falcato, P.; Bertolo, J. M.; Bearzotti, A.; Amenitch, H. *J. Non-Cryst. Solids* **2005**, *351*, 1980–1986.

(10) Jiang, Y.-B.; Liu, N.; Gerung, H.; Cecchi, J. L.; Brinker, C. J. *J. Am. Chem. Soc.* **2006**, *128*, 11018–11019.

that, using short chain ( $C_6$ ) phospholipids, nanostructured films formed via an EISA process can be coassembled with living cells, to create a biocompatible encapsulation matrix for whole-cell biosensor devices<sup>11</sup> that preserves cell viability for months under desiccating conditions. Because the surfactants typically used for the EISA process are either nonbiocompatible (e.g., ionic surfactants such as cetyltrimethylammonium bromide) or do not form high quality films and/or mesophases with extended order in the pH range needed for cell viability (block copolymers)<sup>5</sup>, we introduced the use of short-chain zwitterionic phospholipids as templates for nanostructured materials useful for encapsulation of whole cells, specifically *Saccharomyces cerevisiae*. It was hypothesized that the zwitterionic headgroup would minimize electrostatic interactions with the cell membrane (thus increasing cell viability), while shorter acyl chains (6–10 carbons, in comparison to typical cell membrane phospholipids that often contain 18 or more carbons) would increase the template solubility in the alcohol and water media necessary for sol–gel chemistry and because of their reduced packing parameters<sup>4</sup> promote the formation of higher curvature hexagonal and cubic mesophases. Not only was the biocompatibility of lipid templates confirmed (with cells encapsulated within lipid/silica mesophases actually experiencing increased viability relative to cells encapsulated within films of pure silica)<sup>11</sup> but also the presence of cells was found to actively alter the self-assembly pathway of the lipid/silica mesophase, providing a method of localizing lipids plus any added proteins or nanocrystals at the cell/inorganic interface,<sup>11</sup> thereby enabling engineering of the cell/nanostructure interface.

For continuation of these studies on cell-directed self-assembly, however, a better understanding of the relationship between the molecular structure of the phospholipid SDA and the resulting lipid/silica mesophase is needed. Although the bulk phase diagrams of short-chain phospholipids in water have not been studied in detail (especially with added soluble silica),<sup>12</sup> a number of analytical techniques have been developed to examine the lyotropic behavior of lipids in general.<sup>13,14</sup> Of these, small-angle X-ray scattering (SAXS) is perhaps the most widely used method for examining the structure of bulk mesophases of not only lipids but also of surfactants and other types of self-assembling molecules. However, orientation and distortion of mesophases relative to the substrate during EISA generally prevents the unique assignment of the thin-film mesostructure type from 1D diffraction data.<sup>15</sup> Also, the low scattering volume present in a thin film (ca. 250–500 nm thick) complicates standard SAXS analysis. To bypass these issues, we utilized grazing incidence small-angle X-ray scattering (GISAXS), performed at a high-intensity synchrotron source with a 2D detector, to characterize the static phase behavior of various (short-chain) phospholipids in silica films formed via the combination of sol–gel chemistry and EISA. In GISAXS, the X-ray beam is incident upon the sample at an angle greater than the critical angle of the film, but less than that of the substrate, maximizing the scattering volume and enabling the investigation of nanostructure in films as thin as one monolayer. Unlike electron microscopy, a large area of the substrate is

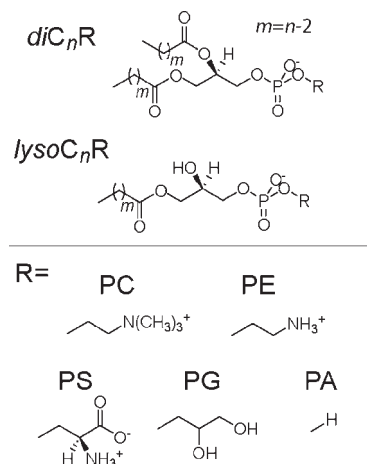


**Figure 1.** Structures of phospholipids investigated as silica templates in films synthesized via EISA. PC, phosphatidylcholine; PE, phosphatidylethanolamine; PS, phosphatidylserine; PG, phosphatidylglycerol; PA, phosphatidic acid.

interrogated, yielding an overall average (representative) structure of the film.

More specifically, the effect of acyl chain length in diacyl phosphatidylcholines on mesophase structure in lipid/silica films synthesized using EISA, as well as the effect of headgroup identity for diacyl phospholipids of constant tail length (six carbons), was investigated. To increase the range of phases formed by phospholipids to include 3D micellar phases, we examine the templating behavior of monoacyl phosphatidylcholines (so-called lysolipids) in addition to diacyl phospholipids. We also compare lipid-templated silica materials with materials formed using a hybrid precursor (bis(triethoxysilyl)ethane). For these various lipid/silica mesophases, we characterize the pore structure of films obtained after solvent extraction (in 3D mesophases formed from phospholipids) or thermal calcination (for lipid-templated hybrid films). We also examine the effect of phospholipids on framework condensation using vibrational spectroscopy and NMR and find that these lipids suppress the condensation of silica but enhance the reactivity of the hybrid framework. Finally, 1D X-ray scattering and FTIR data are found to be consistent with the presence of strong interactions between lipids and the framework phase.

## Experimental Section

In a typical film preparation, 20–50 mg of lipid, 0.122 mL of tetraethyl orthosilicate (TEOS), and 0.16 mL of 0.05 M HCl were added to 0.6 mL of ethanol. This sol was aged for 10 min at room temperature before spin coating at 2000 rpm in a glovebox environment kept at a relative humidity of 15–20% through a flow of dry N<sub>2</sub>. For the synthesis of lipid/bis(triethoxysilyl)ethane (BTESE) films, 69  $\mu$ L of BTESE replaced the TEOS in the above formulation, maintaining the same lipid/silicon ratio for both recipes. All lipids were purchased from Avanti Polar Lipids in dry form and were used as received. TEOS (98%), BTESE, and HCl were purchased from Aldrich; absolute ethanol was obtained from Aaper.

The structures of the phospholipid templates investigated in this article are given in Figure 1. We adopt a nomenclature where the prefix *di-* or *lyso-* signifies lipids with one or two acyl tails, respectively, the subscript *n* in C<sub>n</sub> gives the number of carbon atoms in each acyl chain, and the type of headgroup is identified by the suffix (PC = phosphatidylcholines; PE = phosphatidylethanolamine; PS = phosphatidylserine; PG = phosphatidylglycerol; PA = phosphatidic acid).

Because the final mesostructure is largely determined by the surfactant/oxide volume ratio in nanostructure films synthesized

(11) Baca, H. K.; Ashley, C.; Carnes, E.; Lopez, D.; Flemming, J.; Dunphy, D.; Singh, S.; Chen, Z.; Liu, N.; Fan, H.; Lopez, G. P.; Brozik, S. M.; Werner-Washburne, M.; Brinker, C. J. *Science* **2006**, *313*, 337–341.

(12) Koyanova, R.; Caffrey, M. *Chem. Phys. Lipids* **2002**, *115*, 107–219.

(13) Kleinschmidt, J. H.; Tamm, L. K. *Biophys. J.* **2002**, *83*, 994–1003.

(14) (a) Oradd, G.; Gustafsson, J.; Almgren, M. *Langmuir* **2001**, *17*, 3227–3234. (b) Pitzalis, P.; Monduzzi, M.; Krog, N.; Larsson, H.; Ljusberg-Wahren, H.; Nylander, T. *Langmuir* **2000**, *16*, 6358–6365. (c) Qiu, H.; Caffrey, M. *Biomaterials* **2000**, *21*, 223–234.

(15) Tate, M. P.; Urade, V. N.; Kowalski, J. D.; Wei, T.; Hamilton, B. D.; Egginan, B. W.; Hillhouse, H. W. *J. Phys. Chem. B* **2006**, *110*, 9882–9892.

using an EISA process, we report the amount of lipid added to each formulation relative to the amount of silica present in the sol. For experimental convenience, this ratio is given as mg of lipid per mmol of silica, the latter figure given in molar units to facilitate conversion of the above recipe to sols with different silica precursors (e.g., BTESE).

GISAXS measurements were performed on beamline 8-ID at the Advanced Photon Source at Argonne National Laboratories using a wavelength of 1.6868 Å, a sample-to-detector distance of either 1580 or 1254 mm, and a 2048 × 2048 Marr CCD detector. Reflectivity measurements were used to position the sample angle in the range above the critical angle of the film but below that of the substrate, the criterion for grazing incidence; typical analysis angles were 0.18–0.20°. NANOCELL,<sup>15</sup> a program developed at Purdue University for analysis of SAXS and GISAXS data of nanostructured materials, was used to fit the resulting 2D scattering data.

X-ray diffraction (XRD) was performed on a PANalytical X'pert Pro system equipped with an X'Celerator detector. Refractive index and thickness measurements were made with a J.A. Wollam Co. M44 spectroscopic ellipsometer using a Cauchy dispersion model to determine film optical constants. Refractive index profiles were assumed to be step-index, corresponding to a homogeneous film structure. All refractive index values (reported at a wavelength of 632.5 nm) and thickness measurements were made in triplicate and averaged to obtain the data points reported herein.

Nitrogen adsorption isotherms were collected using an in-house designed 96 MHz surface acoustic wave (SAW) apparatus interfaced with a Micromeritics ASAP 2020 surface area and porosimetry analyzer.<sup>16</sup> Films were deposited on SAW substrates under conditions identical to those used for films made for ellipsometric and X-ray analysis.

TEM was performed on a JEOL 2010, operating at an accelerating voltage of 200 kV and equipped with a Gatan slow scan CCD camera. TEM samples were prepared by scraping the film with a sharp blade and transferring the flakes to a carbon-coated copper grid. Imaging was performed in under-focus conditions. For FTIR studies, films were deposited onto undoped silicon substrates and analyzed in a transmission geometry using a Bruker Vector 22 spectrometer. Confocal and phase contrast images of *diC*<sub>10</sub>PC/silica films were taken with a BioRad Radiance 2100 confocal microscope using the 488 nm line of a 5 mW Ar laser source.

High resolution solution <sup>29</sup>Si NMR spectra were obtained on a Bruker DRX400 instrument at 79.50 MHz using a 10 mm low <sup>29</sup>Si background probe, quartz tubes, and an inverse gated pulse sequence. To reduce the spin–lattice relaxation rates, CrAcAc was added to the solution, with a final concentration of 1 mM. The hydrolysis kinetics were followed using 32 to 86 scan averages with a 20 s recycle delay. The <sup>29</sup>Si chemical shifts were referenced to external TMS  $\delta = 0.0$  ppm. The assignment of the different hydrolysis species was based on previous results.<sup>17</sup>

The solid state <sup>29</sup>Si and <sup>31</sup>P magic angle spinning (MAS) NMR spectra were obtained on a Bruker Avance 400 instrument at 79.50 MHz and 171.99 using a 4 mm broad-band probe spinning between 4 and 12.5 kHz. The <sup>29</sup>Si cross-polarization (CP) spectra were obtained with a 5 ms contact pulse and a 5 s recycle delay, while the direct single pulse Bloch decay was obtained with a 240 s recycle delay. The <sup>29</sup>Si NMR chemical shifts were referenced to the secondary standard Q<sub>8</sub>M<sub>8</sub> ( $\delta = +11.5$  ppm with respect to TMS  $\delta = 0$  ppm). The solid state <sup>31</sup>P MAS NMR spectra were obtained using a single pulse Bloch decay with a 20 s recycle delay. The <sup>31</sup>P chemical shifts were referenced to the secondary external standard H<sub>2</sub>NH<sub>4</sub>PO<sub>4</sub> ( $\delta = 0.8$  ppm with

respect to 85% phosphoric acid at  $\delta = 0.0$  ppm). All spectra were obtained using high power <sup>1</sup>H TPPM decoupling.<sup>18</sup> The spectral deconvolutions and fitting of the <sup>31</sup>P chemical shift anisotropy (CSA) tensor and isotropic chemical shift were performed in the DMFIT program.<sup>19</sup>

## Results and Discussion

Previously, for use in cell-directed assembly, a stock solution containing prehydrolyzed and partially condensed silica oligomers was used to synthesize lipid-templated silica films. This approach can suffer from poor reproducibility of overall film and nanostructure quality, however, because of the difficulty in controlling the degree of condensation during the stock synthesis combined with continuing reaction of the oligomers during stock storage, even at low temperatures.<sup>20</sup> Instead, for these studies we use direct addition of the silica precursor, TEOS, to the synthesis solution, followed by hydrolysis at room temperature (20 °C) for 10 min before film coating. Although all experimental data reported here is from films deposited after this 10 min sol aging period, extended aging under ambient conditions for up to 3 h was found to have no effect on macroscopic film quality and nanoscale order, as determined by coating a film every 15 min from a sol maintained at room temperature. Overall film homogeneity was not affected, with the only observable effect on nanostructure being a small increase in lattice spacing with time (an effect of an increase in silica oligomer size during sol aging).<sup>20</sup>

In addition to silica condensation, lipid degradation under acidic conditions (such as that found in the precursor sol) may impact film quality. We followed the degradation of the headgroup in *diC*<sub>6</sub>PC under typical sol conditions (i.e., 0.10 M HCl) using <sup>31</sup>P and <sup>1</sup>H solution state NMR. After 16 h, only ca. 4% of phosphorus centers had undergone a change in chemical state, with no significant changes in the <sup>1</sup>H spectrum observed after HCl addition.

**Diacyl Phosphatidylcholine Templates.** Ideally, a lipid/silica mesophase used for cell entrapment will possess an extended, continuous 3D structure such that template removal creates a continuous 3D pore network with long-range pathways for facile mass transport throughout the film. Identifying both a lipid structure and lipid/silica ratio that yields such a mesophase using *a priori* prediction is difficult, however; the critical packing parameter *g*, defined by  $g = v/a_0l_c$  (where *v* = volume of the lipid tail, *a*<sub>0</sub> = optimal headgroup area, and *l*<sub>c</sub> = the critical chain length of the lipid tails), is commonly used to describe the aggregation morphology of self-assembling amphiphiles<sup>4</sup> but is unable to fully predict lipid/water phase diagrams.<sup>2,21</sup> More advanced (computational) models are also generally limited to qualitative descriptions of lipid/water mesostructure.<sup>22</sup> We thus adapt an empirical approach to mapping out the relationships between lipid structure, lipid/silica ratio, and type of mesostructure formed, first investigating mesophase formation as a function of chain length in diacyl phosphatidylcholines, and then, keeping the tail length constant, investigating the effect of headgroup identity.

We first investigated the effect of lipid tail length for the dialkyl phosphatidylcholines *diC*<sub>6</sub>PC, *diC*<sub>8</sub>PC, and *diC*<sub>10</sub>PC

(19) Massiot, D.; Fayon, F.; Capron, M.; King, I.; Le Calve, S.; Alonso, B.; Durand, J.-O.; Bujoli, B.; Gan, Z.; Hoatson, G. *Magn. Reson. Chem.* **2002**, *40*, 70–76.

(20) Brinker, C. J.; Scherer, G. W. *Sol-Gel Science: The Physics and Chemistry of Sol-Gel Processing*; Academic Press: San Diego, CA, 1990.

(21) Mezzenga, R.; Schurtenberger, P.; Burbridge, A.; Michel, M. *Nat. Mater.* **2005**, *4*, 729–740.

(22) Mezzenga, R.; Lee, W. B.; Fredrickson, G. H. *Trends Food Sci. Technol.* **2006**, *17*, 220–226.

(16) Ricco, A. J.; Frye, G. C.; Martin, S. J. *Langmuir* **1989**, *5*, 273–276.

(17) Alam, T. M.; Henry, M. *Phys. Chem. Chem. Phys.* **2000**, *2*, 23–28.

(18) Bennett, A. E.; Rienstra, C. M.; Auger, M.; Lakshmi, K. V.; Griffin, R. G. *J. Chem. Phys.* **1995**, *103*, 6951–6958.



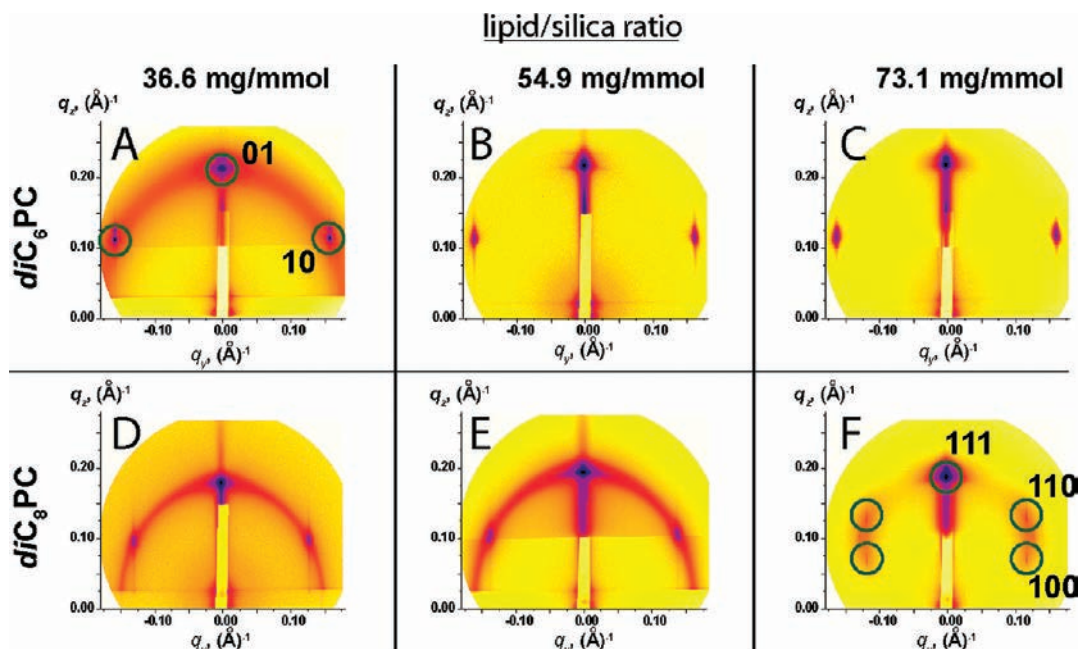


**Figure 2.** GISAXS patterns for  $diC_6PC$  (A–C) and  $diC_8PC$ -templated (D–F) silica as a function of the lipid/silica ratio. Data for  $diC_6PC$  at a lipid/silica ratio of 36.6 mg/mmol is indexed to a 2D hexagonal mesophase, while the data for  $diC_8PC$  at a lipid/silica ratio of 73.1 mg/mmol is indexed to rhombohedral space group  $R-3m$ .

on lipid/silica film structure over a lipid/silica ratio range of ca. 30–100 mg/mmol. This corresponds to an approximate lipid volume fraction in hydrated, as-deposited films of 30–60% (assuming a density of 1.0 g/mL for the lipid phase).<sup>5</sup> This range was selected to match the range of surfactant/silica ratios generally used in films templated with synthetic amphiphiles.<sup>2</sup>

Estimates of  $g$  for the diacyl lipids (ca. 0.45 ( $C_6$ ) to 0.55 ( $C_{10}$ ))<sup>13</sup> predict that nonspherical micelles (e.g., hexagonal rods) will dominate the diacyl lipid/ $H_2O$  phase diagram.<sup>4</sup> This is confirmed for  $diC_6PC$  by the GISAXS data given in Figure 2A–C for lipid/silica ratios between 36.6 and 73.1 mg/mmol  $SiO_2$ . However, pure  $diC_6PC$ , when cast as a film from an ethanol solution, yields a lamellar phase with interplanar spacing of 25.3 Å; lamellar phases were also observed in  $diC_6PC$ /silica films for ratios greater than ca. 80 mg/mmol. Some loss of orientational order can be seen at low lipid/silica ratios, as evidenced by the appearance of a diffuse ring in the GISAXS scattering pattern (Figure 2A). All patterns show uniaxial shrinkage of the nanostructure of ca. 15% in the direction normal to the substrate from silica condensation during film drying (from an undistorted {01} spacing of 35 Å, determined by the position and angle of the (10) reflection relative to the  $q_y$  axis).

A 2D hexagonal structure is also observed for  $diC_8PC$ -templated silica between lipid/silica ratios of 36.6 and 54.9 mg/mmol (Figure 2D–E), with an undistorted {01} spacing of 40 Å. Compared to  $diC_6PC$ , the degree of orientational order of the  $diC_8PC$ /silica mesophase is lower, with a diffuse ring present in the GISAXS patterns over the entire compositional range where a 2D hexagonal phase is present. At the lipid/silica ratio for  $diC_8PC$ -templated films shown in Figure 2F, a new pattern appears that we fit to a  $[111]$ -oriented rhombohedral space group ( $R-3m$ ;  $a = 45$  Å;  $\alpha = 75^\circ$ ) using NANOCELL. Although this mesophase could comprise close-packed monodisperse micelles, (the rhombohedral symmetry being derived from distortion of face-centered cubic packing)<sup>23</sup>, the size of micellar aggregates

typically formed by  $diC_8PC$  (MW  $\approx 1\text{--}2 \times 10^6$  g/mol,<sup>24</sup>  $r \approx 7\text{--}9$  nm, assuming purely spherical micelles) is not consistent with the fitted unit cell parameters, assuming close-packed micelles. Another potential rhombohedral structure for this film is that of a membrane fusion intermediate whereby hourglass-shaped stalks link adjacent lipid bilayers;<sup>25</sup> this phase has been postulated to exist as a transition state in membrane fusion and has been characterized for a methylated analogue of dipalmitoyl phosphatidylcholine. As with  $diC_6PC$ ,  $diC_8PC$  forms lamellar phases with silica at lipid/silica ratios above 80 mg/mmol (pure  $diC_8PC$  also adopts a lamellar structure, with an interplanar spacing of 30.4 Å).

For  $diC_{10}PC$ , complete phase separation between the lipid and silica occurs during the EISA process. X-ray scattering data shows no significant difference in lattice spacing between pure  $diC_{10}PC$  (lamellar structure,  $d = 34$  Å) and lipid/silica composites ( $d = \text{ca. } 35$  Å). Furthermore, confocal microscopy (Figure 3A) of a  $diC_{10}PC$ /silica film doped with a polar fluorescein derivative that selectively partitions into the hydrophilic silica framework shows complete macroscopic phase separation between the two components; holes in the fluorescence image correspond to what appear to be globules of lipid in the phase contrast image.

Phase separation of  $diC_{10}PC$  is consistent with the trend in critical micelle concentration ( $cmc$ ) for dialkyl phosphatidylcholines; the  $cmc$  for  $diC_nPC$  decreases dramatically as  $n$  increases, with the  $cmc$  for  $n = 6, 8$ , and  $10$  being 15.4, 0.16, and 0.009 mM, respectively.<sup>26</sup> This rapid decrease of  $diC_nPC$  solubility as the tail is lengthened may also account for the loss of orientational order seen in 2D hexagonal phases for  $diC_8PC$ ; during film evaporation, rapid kinetics of mesophase formation will induce the formation of unoriented nanostructures (i.e., favoring precipitation over alignment by the solid/liquid or liquid/air interfaces).

(24) Tausk, R. J. M.; Oudshoorn, C.; Overbeek, J. T. G. *Biophys. Chem.* **1974**, *2*, 53–63.

(25) Yang, L.; Huang, H. W. *Biophys. J.* **2003**, *84*, 1808–1817.

(26) Weshayanwivat, P.; Scamehorn, J. F.; Reilly, P. J. *J. Surfactants Deterg.* **2005**, *8*, 65–72.

(23) Eggiman, B. W.; Tate, M. P.; Hillhouse, H. W. *Chem. Mater.* **2006**, *18*, 723–730.

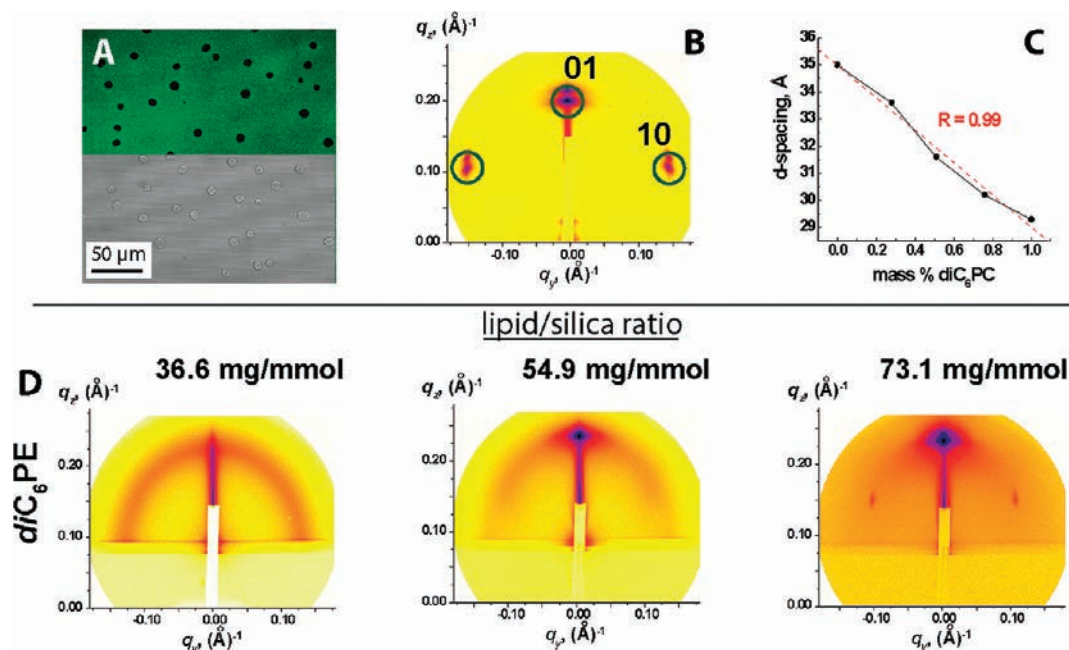


**Figure 3.** (A) Confocal/phase contrast image of a fluorescein-doped  $diC_8PC/SiO_2$  film, showing phase separation of the lipid. (B) GISAXS image of a 2D hexagonal phase obtained from a mixture of  $diC_6PC$  and  $diC_8PC$  in  $SiO_2$ . (C) The relationship between interplanar spacing and mass ratio of  $diC_6PC$  and  $diC_8PC$  in lipid-templated films. (D) GISAXS patterns for  $diC_6PE$ -templated silica as a function of the lipid/silica ratio.

Because blends of lipids can be used to modify phase diagrams or the physical properties of particular phases, we examined silica templating by binary mixtures of  $diC_6PC$  and  $diC_8PC$ . Over the entire range of  $diC_6PC/diC_8PC$  ratios, nanostructures with 2D hexagonal symmetry (Figure 3B) were observed, with lattice spacing (as determined by XRD, Figure 3C) being linearly proportional to this ratio.

Removal of the PC lipid template from these nanostructured films was attempted with thermal calcination as well as  $UV/O_3$  treatment. However, complete film collapse was obtained in all experiments, even after film aging, heating, or treatment with  $NH_3$  or  $HCl$  vapor to increase the degree of silica condensation. Solvent extraction of the lipid was also ineffective, presumably due to poor accessibility of the lipid mesophase to the surface of the film or strong lipid/silica interactions. TEM analysis of the nanostructured film showed no characteristic structure, likely an effect of damage from the electron beam coupled with the small feature size of the lipid nanostructure.

#### Effect of the Lipid Headgroup on Mesophase Formation.

Although phosphatidylcholines are prevalent in many biological membranes, a diverse range of headgroup structures are found in nature, each with unique chemical properties (acidity, charge, hydrogen bonding ability, etc.). We investigated the effect of this headgroup chemistry on mesophase formation by synthesizing lipid/ $SiO_2$  films with  $diC_6PE$ ,  $diC_6PG$ ,  $diC_6PS$ , and  $diC_6PA$  templates under conditions identical to those used for  $diC_6PC/SiO_2$  films. While the templates  $diC_6PS$  and  $diC_6PA$  produced films of poor macroscopic quality at all lipid/silica ratios,  $diC_6PE$  and  $diC_6PG$  did yield homogeneous films (for  $diC_6PG$ , spin coating at 4000 rpm was used to compensate for an increased solution viscosity due to the glycerol headgroup); the relative degree of nanostructure order was reduced with these two lipid templates in comparison with that of  $diC_6PC$ , however. Figure 3D shows GISAXS data for  $diC_6PE$  films with lipid/silica ratios of 36.6 to 73.1 mg/mmol  $SiO_2$ . At low lipid concentrations, a diffuse ring indicates a lack of long-range and orientational order. Although this scattering pattern could be interpreted as a

worm-hole-type mesostructure, the possibility of a nonoriented lamellar phase cannot be excluded. As the amount of lipid is increased, a strong reflection from planes parallel to the substrate surface appears, while diffuse scattering is present in the region of the detector where  $\{10\}$  reflections would be expected for a 2D hexagonal phase; this diffuse scattering becomes better defined into a  $\{10\}$  reflection at a lipid/silica ratio of 73.1 mg/mmol. The relative weakness of these spots, however, compared to the reflection at  $q_y = 0$  suggests that a lamellar phase is predominant in comparison to the hexagonal structure. Scattering data for  $diC_6PG$  is essentially identical. As was seen for  $diC_6PC$  and  $diC_8PC$ , removal of  $diC_6PE$  or  $diC_6PG$  by thermal calcination or  $UV/O_3$  degradation resulted in the collapse of the film, while solvent extraction did not yield any template removal.

**Lysophosphatidylcholine Templates.** An alternate strategy to using diacyl PCs with short alkyl tails to improve template solubility in polar solvents is to remove one alkyl chain from otherwise insoluble lipids, forming what are termed lysolipids. As an example of the solubility increase attained from this structural modification, the *cmc* of  $lysoC_{10}PC$  is 6.0 mM,<sup>27</sup> compared to only 0.009 mM for  $diC_{10}PC$ . Also, elimination of one acyl chain reduces the tail volume by 50%, reducing  $g$  to below 0.3, a range where micellar mesophase formation is expected.<sup>4</sup> Published phase diagrams for these lipids do indeed show the presence of micellar cubic phases that could potentially be used to template 3D porosity in EISA-derived silica films.<sup>28</sup>

We investigated lysolipids with the general formula  $lysoC_nPC$  (Figure 1) for  $n = 6, 10, 12, 14$ , and 16. When  $n = 6$ , no ordered mesophase is observed for lipid-templated silica (although the pure lipid crystallizes into a 2D hexagonal phase, with the lattice parameter  $a = 24.8$  Å). For the other lipids, structured mesophases are obtained over the lipid/silica ratio of 47.8 to 83.9 mg/mmol  $SiO_2$ . GISAXS of these films shows that the phase

(27) Stafford, R. E.; Dennis, E. A. *Colloids Surf.* **1988**, *30*, 47–64.

(28) Arvidson, G.; Brentel, I.; Khan, A.; Lindblom, G.; Fontell, K. *Eur. J. Biochem.* **1985**, *152*, 753–759.

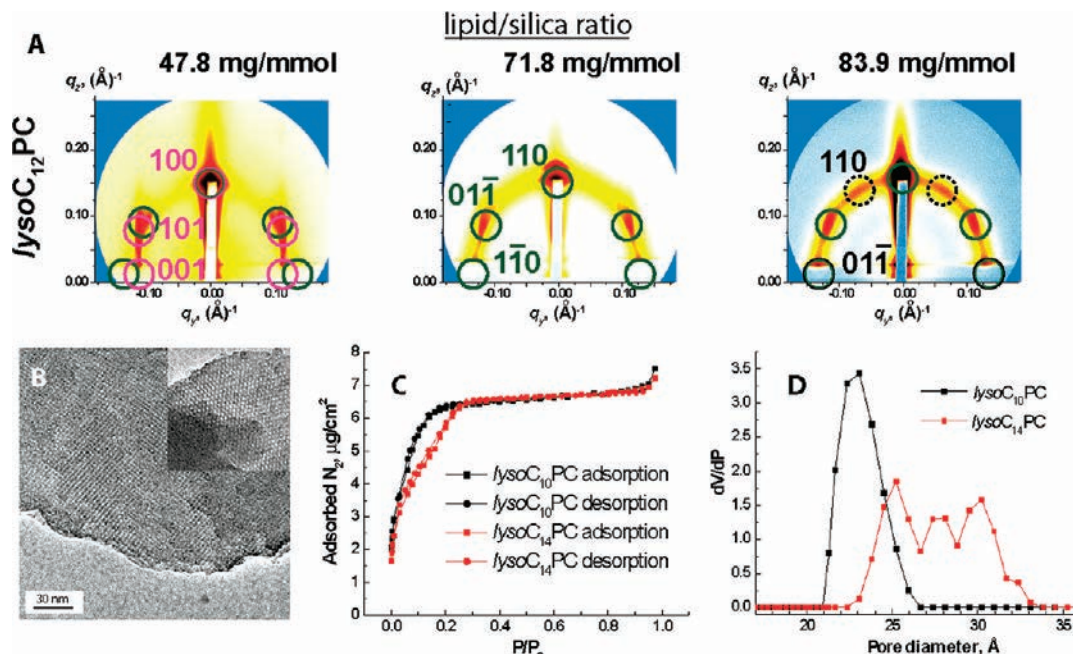


**Figure 4.** (A) GISAXS patterns for *lysoC*<sub>12</sub>PC-templated silica as a function of the lipid/silica ratio, indexed as green, [110] oriented *Im*-3m; pink, [100] oriented *P6*<sub>3</sub>/mmc; black dashed line, [111] oriented *Im*-3m. (B) [001]-oriented TEM image of *lysoC*<sub>14</sub>PC-templated silica after solvent extraction. (C) N<sub>2</sub> adsorption isotherms for *lysoC*<sub>14</sub>PC and *lysoC*<sub>10</sub>PC-templated SiO<sub>2</sub> films. (D) Pore size distributions calculated from the adsorption branch of these isotherms.

behavior is similar for all values of  $n$  between 10 and 16; Figure 4A contains typical scattering data for *lysoC*<sub>14</sub>PC at lipid/silica ratios of 47.8, 71.8, and 83.9 mg/mmol SiO<sub>2</sub>. At the lowest lipid concentration, a mixture of phases is observed that we fit to two structures obtained from the packing of spherical micelles: [001]-oriented 3D hexagonal (space group *P6*<sub>3</sub>/mmc,  $a = b = 65$  Å,  $c = 80$  Å) and another phase consistent with either *Pm*-3n or *Im*-3m symmetry, oriented with the [110] direction orientation parallel to the substrate normal and  $a = 65$  Å (but distorted by ca. 30% perpendicular to the substrate surface due to uniaxial shrinkage during film drying). While the 3D hexagonal phase has not been observed previously in any lysolipid/water phase diagram, the *Pm*-3n structure has been well characterized with a body-centered unit cell containing an additional two micelles on each face of the cube.<sup>29</sup> However, we tentatively assign the structure to *Im*-3m upon the basis of the unit cell parameter; in the *lysoC*<sub>16</sub>PC/water system,  $a =$  ca. 125 Å for the *Pm*-3n phase,<sup>29</sup> while we only measure  $a =$  ca. 70 Å in *lysoC*<sub>16</sub>PC/silica films. Given the lack of higher-order diffraction features in the data from Figure 4, vigorous differentiation between *Pm*-3n and *Im*-3m is not possible at this time.

As the amount of lipid is raised relative to that of silica, the 3D hexagonal phase becomes less pronounced, eventually disappearing at ca. 71.8 mg lipid/mmol SiO<sub>2</sub>, where a loss of orientational order (as evidenced by the appearance of a diffuse ring) is observed, accompanied by the appearance of extra reflections to each side of the (110) diffraction spot. Although a lack of reflections outside the diffuse ring prevents the definitive assignment of these features, these new spots are consistent with the presence of [111]-oriented *Im*-3m domains with the same 30% contraction normal to the substrate found for the [110] orientation. *LysoC*<sub>12</sub>PC and *lysoC*<sub>16</sub>PC both feature the same phase behavior as that shown for *lysoC*<sub>14</sub>PC; *lysoC*<sub>10</sub>PC, however, differs in that a diffuse ring and the (111) reflections are seen

for all lipid/SiO<sub>2</sub> concentrations, indicating a lack of orientation order relative to that of other lysolipids with longer acyl tails.

As was seen for the diacyl PCs, removal of the lipid template by thermal calcination or UV/O<sub>3</sub> treatment resulted in complete collapse of film porosity. However, solvent extraction in 0.01 M HCl in ethanol for 2 days at 50 °C did yield porous films with total pore volumes of ca. 35–40% (as estimated by spectroscopic ellipsometry). Significant stresses were developed in films during lipid removal, as evidenced by extensive cracking after removal from the extraction solution. N<sub>2</sub> adsorption isotherms for *lysoC*<sub>10</sub>PC-, *lysoC*<sub>12</sub>PC-, and *lysoC*<sub>14</sub>PC-templated films were measured on SAW devices after extraction of the lipid. Figure 4C shows isotherms for *lysoC*<sub>10</sub>PC/SiO<sub>2</sub> and *lysoC*<sub>14</sub>PC/SiO<sub>2</sub> films; the former is indicative of a microporous material (using IUPAC terminology, a type I isotherm), while the *lysoC*<sub>14</sub>PC/SiO<sub>2</sub> film yielded a type IV (mesoporous) isotherm. Both sets of data show a small upturn at high partial pressure from macroporosity created by cracking of the film. Pore size distributions (PSD, Figure 4D) show a narrow (ca. 7 Å wide) pore size distribution for the *lysoC*<sub>10</sub>PC-templated film centered at 23 Å, while the significantly broader distribution (about 11 Å) for the *lysoC*<sub>14</sub>PC/SiO<sub>2</sub> film is centered at 27.5 Å; why this lipid shows a wider PSD is unknown at this time. The calculated distribution for a *lysoC*<sub>12</sub>PC/SiO<sub>2</sub> film (data not shown) is similar to that for the *lysoC*<sub>10</sub>PC-templated material, with a PSD of  $24.5 \pm 4$  Å.

TEM analysis after lipid extraction (Figure 4B) shows nanostructure consistent with micellar packing, with planes of both 4-fold and 3-fold symmetry. Although the former indicates the presence of a cubic phase, 3-fold symmetry can be obtained from either cubic or 3D hexagonal phases (both of which were identified in *lysoC*<sub>14</sub>PC/SiO<sub>2</sub> films by GISAXS).

**Lipid/Bis(triethoxysilyl)ethane Films.** In addition to our investigations of lipid/silica film structure, we also examined the templating behavior of lipids when TEOS was substituted by the hybrid silsesquioxane precursor BTESE. Bridged silsesquioxanes such as BTESE are readily incorporated into the framework of films synthesized using EISA, introducing covalently linked

(29) Eriksson, P.-O.; Lindblom, G. *J. Phys. Chem.* **1987**, *91*, 846–853.



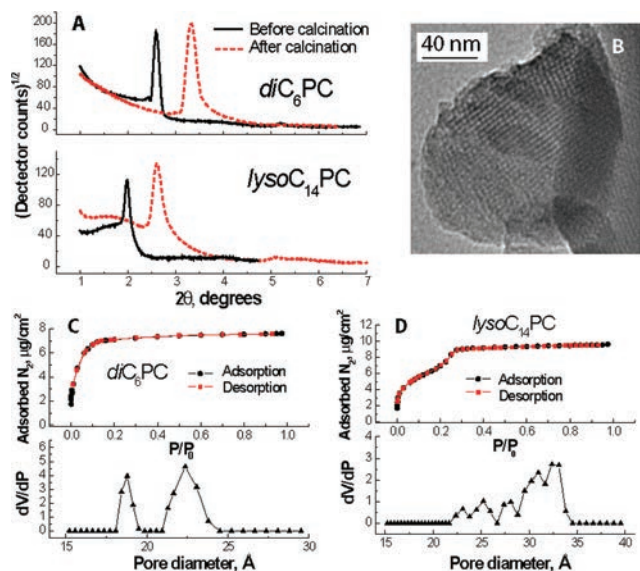


**Figure 5.** (A) XRD data for *diC*<sub>6</sub>PC and *lysoC*<sub>14</sub>PC-templated BTESE films, before and after thermal calcination. (B) TEM image obtained from a calcined *lysoC*<sub>14</sub>PC-templated BTESE film. (C) N<sub>2</sub> adsorption isotherm and pore size distribution for a *diC*<sub>6</sub>PC-templated BTESE film. (D) N<sub>2</sub> adsorption isotherm and pore size distribution for a *lysoC*<sub>14</sub>PC-templated BTESE film.

organic functionality into the inorganic network.<sup>7,30</sup> Porous hybrid materials synthesized with hybrid precursors exhibit new properties, including increased hydrolytic stability relative to materials of pure silica,<sup>31</sup> a critical property for interfacing lipid-templated films with biological systems at near-neutral pH and high ionic strength.

Lipid-templated BTESE films were synthesized under identical conditions to those used for films made with the purely inorganic precursor TEOS; the EISA precursor solution was only modified by replacing TEOS with BTESE in a 2:1 mol ratio (maintaining a constant Si/lipid ratio in the two systems). Figure 5A shows XRD data for as-deposited *diC*<sub>6</sub>PC/BTESE and *lysoC*<sub>14</sub>PC/BTESE films (using a lipid/Si molar ratio of 71.8 mg/mmol for both cases) and indicates that mesoscale order is maintained when TEOS is replaced with BTESE, with interplanar spacing in each case being similar to those obtained when using the TEOS precursor alone. GISAXS patterns of the *diC*<sub>6</sub>PC/BTESE films show that the *p*<sub>6</sub>mm 2D hexagonal structure is maintained; for *lysoC*<sub>14</sub>PC/BTESE, TEM data (Figure 5B) is consistent with the cubic phase seen previously with *lysoC*<sub>14</sub>PC/SiO<sub>2</sub> films.

Unlike PC/SiO<sub>2</sub> films, however, the nanostructure of these films was preserved during the removal of the lipid template by thermal pyrolysis. Films were placed in a 350 °C oven for 30 min; this temperature was selected to minimize degradation of Si-CH<sub>2</sub>CH<sub>2</sub>-Si functionality within the hybrid framework. After removal of the lipid, the refractive index at 630 nm of *diC*<sub>6</sub>PC- and *lysoC*<sub>14</sub>PC-templated films was reduced from 1.47 and 1.51 to 1.30 and 1.22, respectively, demonstrating the formation of a porous material. Film thickness was reduced by ca. 15–25% for each film due to uniaxial shrinkage of the film resulting from silica condensation, with the *d*-spacing for the planes of the nanostructure parallel to the substrate surface being reduced by a similar amount (Figure 5A). In addition to stability toward lipid removal by calcination, solvent extraction of *lysoC*<sub>14</sub>PC/BTESE films

produced porous films with no cracking. UV/O<sub>3</sub> treatment of these films led to complete collapse of porosity, presumably a result of a lack of selectivity for the reaction of O<sub>3</sub> between the lipid template and the integrated organic framework functionality.

*DiC*<sub>6</sub>PC/BTESE and *lysoC*<sub>14</sub>PC/BTESE films were prepared on SAW substrates for N<sub>2</sub> adsorption analysis and calcined at 350 °C as described above. Figure 5C and D shows the isotherms obtained from these samples, along with pore size distributions obtained by fitting the data with a DFT-based model.<sup>32</sup> The isotherm for the *diC*<sub>6</sub>PC/BTESE film is indicative of a microporous material (a type I isotherm), consistent with the expected diameter of cylindrical micelle based upon the thickness of a *diC*<sub>6</sub>PC bilayer (ca. 25 Å), after accounting for film shrinkage. Deconvolution of this isotherm yields a bimodal distribution, with ca. 60% of the pores in the expected size range (diameter = 22.5 Å) and the remainder in a narrow range around 18 Å. The source of the secondary porosity is unknown and remains a topic for future investigation. A BET surface area of 319 m<sup>2</sup>/cm<sup>3</sup> of film volume was calculated for this film, typical of that seen for other mesoporous materials (the surface area is given here in units of area per unit film volume as the density of the hybrid silsesquioxane skeleton is not known). A type IV (mesoporous) isotherm was obtained for the *lysoC*<sub>14</sub>PC film; this isotherm contains a sharper condensation step than that seen for the *lysoC*<sub>14</sub>/SiO<sub>2</sub> isotherm (Figure 4C), with a similar pore size distribution range but a greater concentration of pores at higher diameter. The BET surface area for this film was determined to be 318 m<sup>2</sup>/cm<sup>3</sup> of film volume. The total N<sub>2</sub> adsorbed at high P/P<sub>0</sub> for both of these isotherms (along with film thickness from ellipsometry) yields porosity levels of 26% (*diC*<sub>6</sub>PC) and 31% (*lysoC*<sub>14</sub>PC), lower than the range obtained from ellipsometric data for films on silicon substrates, 40% and 50% (assuming a similar refractive index for the BTESE wall and surfactant phases), an effect of either porosity that is inaccessible to N<sub>2</sub> adsorption or different thicknesses for films deposited on SAW rather than Si substrates.

**Lipid/SiO<sub>2</sub> and Lipid/BTESE Interactions.** The inability to remove phosphatidylcholines from silica films by thermal or UV/O<sub>3</sub> degradation, in addition to the apparent stresses in silica formed by extraction of lysophosphatidylcholine as well as the contrary behavior of lipid/BTESE films, suggests the presence of strong interactions between the lipid template and the framework material. We hypothesized that these interactions suppress the condensation of the silica network in lipid/SiO<sub>2</sub> and undertook an *ex-situ* FTIR/ellipsometric study to monitor the removal of the lipid template as well as development of the siloxane framework as a function of temperature. In this study (Figure 6A), a group of *diC*<sub>6</sub>PC/SiO<sub>2</sub> films (synthesized with a lipid/silica ratio of 54.9 mg/mmol) as well as CTAB/SiO<sub>2</sub> and pure SiO<sub>2</sub> films (synthesized under conditions identical to those for the lipid/SiO<sub>2</sub> films except for the replacement of CTAB for *diC*<sub>6</sub>PC or the omission of any template) were heated at 1 °C/min in a furnace to nearly 400 °C; samples were removed every 50° during this heating ramp for ellipsometric and transmission FTIR analysis. Refractive index data shows no significant changes in *n* for lipid-templated or nontemplated films, whereas a reduction in *n* between 200° and 250° is seen in CTAB-templated samples, corresponding to the removal of the surfactant template to leave a porous film. Thickness data, however, indicates that between

(30) Lu, Y. F.; Fan, H. Y.; Doke, N.; Loy, D. A.; Assink, R. A.; LaVan, D. A.; Brinker, C. J. *J. Am. Chem. Soc.* **2000**, *122*, 5258–5261.

(31) Shylesh, S.; Jha, R. K.; Singh, A. P. *Microporous Mesoporous Mater.* **2006**, *94*, 364–370.

(32) Jaroniec, M.; Kruk, M.; Olivier, J. P.; Kock, S. *Proceedings of the 5th International Symposium on the Characterization of Porous Solids*; Elsevier: Amsterdam, 1999.

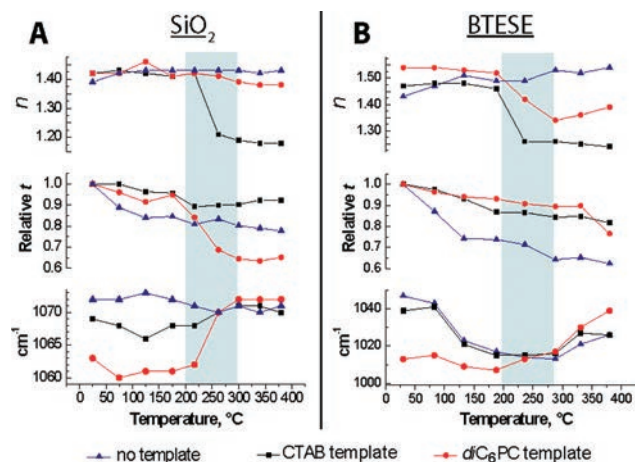


**Figure 6.** *Ex-situ* ellipsometric data (refractive index, relative thickness) and FTIR band position for the  $\nu(\text{Si}-\text{O})$  stretch obtained from films of CTAB-,  $\text{diC}_6\text{PC}$ -, and nontemplated  $\text{SiO}_2$  (A) and BTESE (B) during heating at 1 °C/min.

175° and ca. 250 °C, lipid-templated films collapse as  $\text{diC}_6\text{PC}$  is pyrolyzed (CTAB- and nontemplated films do exhibit some shrinkage, as would be expected from film drying and silanol condensation).

The bottom panel of Figure 6A shows the shift in frequency of the asymmetric Si–O stretch ( $\nu(\text{Si}-\text{O})$ ), correlated with the above changes in film refractive index and thickness. In silica sol–gel materials, the energy of this vibration (occurring at ca. 1070  $\text{cm}^{-1}$ ) has been correlated with the degree of siloxane network connectivity, with the band moving to higher wave numbers with increasing condensation.<sup>20</sup> Initially, the position of the  $\nu(\text{Si}-\text{O})$  band in the CTAB and  $\text{diC}_6\text{PC}$  templated films indicates suppression of condensation relative to that of the nontemplated material, as has been observed previously for surfactant-templated silica films synthesized through EISA.<sup>33</sup> However, this band appears at a significantly lower energy in the films containing  $\text{diC}_6\text{PC}$  when compared to that of CTAB, a feature we ascribe to a lower degree of condensation in films templated with the former. This relative order in  $\nu(\text{Si}-\text{O})$  band energy for the three types of film is reproducible and stable over time; after a period of 10 days, no significant changes in the FTIR spectra are observed, demonstrating that the small differences in sample history (for example, time between film deposition and FTIR data collection) can be ruled out as the source of this observed trend. After  $\text{diC}_6\text{PC}$  removal, above 200°, the frequency of this  $\nu(\text{Si}-\text{O})$  stretch for lipid-templated films converges with that of the other films. We interpret this data as confirmation of our hypothesis; siloxane network formation is suppressed by the presence of lipid, preventing structural stabilization of the pore network as the template is being removed thermally. Although this suppression is also seen for CTAB-templated silica, the effect is not as pronounced.

For lysolipid-templated  $\text{SiO}_2$  films, we posit that the pore network is stabilized toward collapse during lipid removal by extraction by the presence of an acid condensation catalyst, along with the slow extraction rate from the 3D pore network.

Initial condensation state of the CTAB/silica and lipid/silica films were also compared using  $^{29}\text{Si}$  MAS NMR with films scraped from Si wafers. This data, illustrated in Figure 7A, also shows decreased condensation of lipid-templated silica compared to that of the CTAB-templated material, albeit it to a lesser extent. The degree of condensation (DC) for

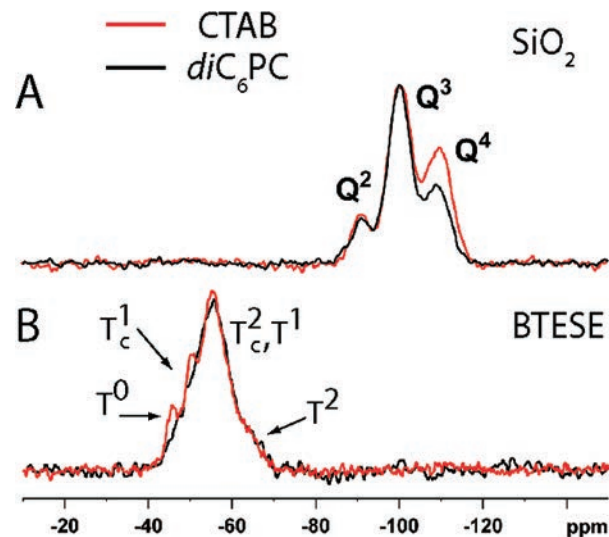


**Figure 7.** Solid-state  $^{29}\text{Si}$  NMR comparing the degree of condensation in CTAB- and  $\text{diC}_6\text{PC}$ -templated  $\text{SiO}_2$  (A) and BTESE (B).

TEOS-derived silica can be defined by

$$DC = \left( \sum nQ^n \right) / 4$$

where  $Q^n$  is the fraction of the different Q species with connectivity  $n$  obtained from fitting the NMR spectra. For the data in Figure 7A, a DC of 0.82 was measured for CTAB/silica, compared to 0.79 for  $\text{diC}_6\text{PC}$ /silica. Although this difference is small, the percentage of Q<sup>4</sup> species in each material supports the interpretation that this difference is significant; %Q<sup>4</sup> for  $\text{diC}_6\text{PC}$ /silica is ca. 25% lower than that for CTAB/silica (27% vs 36%). The smaller differences between lipid- and CTAB-templated materials detected using NMR may reflect a lower sensitivity to long-range network formation when compared with vibrational spectroscopy.

From solution  $^{29}\text{Si}$  NMR, the observed disparity in silica condensation state between the two templates appears to arise during or immediately after the self-assembly process as the initial reaction of TEOS in the template solutions are very similar. Comparison of  $^{29}\text{Si}$  NMR data (see Supporting Information for spectra and assignments) for TEOS, TEOS/CTAB, and TEOS/ $\text{diC}_6\text{PC}$  precursor solutions shows that while the hydrolysis and initial condensation rate of TEOS without any added template are rapid (with hydrolysis nearly complete within the first 40 min), inclusion of CTAB or  $\text{diC}_6\text{PC}$  to the TEOS solution reduces the hydrolysis rate by an identical amount (approximately half) while also slowing the initial condensation rate. While this observed reduction in reaction rates may be an effect of specific intermolecular interactions between template molecules and silica precursors, the increase in ionic strength with template present will decrease solution activities, another possible source of the change in reaction rates.

This ellipsometric/FTIR/NMR study was repeated for  $\text{diC}_6\text{PC}$ -, CTAB- and nontemplated BTESE films (data in Figures 6B and 7B). Refractive index and thickness changes of films during heating are consistent with the removal of both templates to yield porous films, accompanied by shrinkage of the thickness from silanol condensation inside the film. However, the interpretation of shifts in  $\nu(\text{Si}-\text{O})$  bands for BTESE-based films is more complicated than that for  $\text{SiO}_2$ . Above 75°, the frequency of this vibration *decreases*, followed by an increase above 200° (for lipid-templated material) and 300° (for CTAB-templated films as well as nontemplated BTESE). This shift in frequency

(33) Doshi, D. A.; Gibaud, A.; Goletto, V.; Lu, M. C.; Gerung, H.; Ocko, B.; Han, S. M.; Brinker, C. J. *J. Am. Chem. Soc.* **2003**, *125*, 11646–11655.



during heating can be explained by a cyclization reaction for BTESE; this monomer forms a bicyclic intermediate during polymerization that is accompanied by a decrease in stretching frequency (from ca. 1100  $\text{cm}^{-1}$  for the monomer, dropping to ca. 1000–1030  $\text{cm}^{-1}$  upon cyclization).<sup>34</sup> As siloxane network formation proceeds, requiring the opening of the cyclic species, the energy of the  $\nu(\text{Si}-\text{O})$  band again increases<sup>34</sup> to ca. 1040–1080  $\text{cm}^{-1}$ .

Comparison of the  $\nu(\text{Si}-\text{O})$  stretching frequency between *diC*<sub>6</sub>PC and CTAB-templated (as well as nontemplated) BTESE suggests that the presence of the lipid promotes cyclization during film synthesis, as the initial band position before heating is shifted to a lower energy by ca. 30  $\text{cm}^{-1}$  to 1012  $\text{cm}^{-1}$ , within the region in which cyclized species are expected to occur. Also, the onset of the increase in stretching frequency that is correlated with the formation of acyclic species during network polymerization occurs at a lower temperature for lipid-templated films (200 °C) than for CTAB-templated or pure BTESE films (ca. 300 °C). This data indicates that, unlike in pure  $\text{SiO}_2$  films, *diC*<sub>6</sub>PC promotes condensation in the BTESE material.

Solid state <sup>29</sup>Si NMR of as-deposited *diC*<sub>6</sub>PC- and CTAB-templated film material (Figure 7B) is consistent with this model of relative BTESE reactivity. A degree of condensation figure is difficult to calculate for BTESE materials, as cyclic T<sup>2</sup> and acyclic T<sup>1</sup> signals overlap<sup>34</sup> (analogous to the nomenclature for TEOS-based materials, T<sup>n</sup> is the fraction of the different T species with connectivity *n*; the subscript *c* indicates the signal from a cyclized product). Examination of the NMR data, however, clearly shows that CTAB-templated BTESE contains a higher relative contribution from T<sup>0</sup> and T<sup>1</sup> (cyclized) species than lipid-templated BTESE, consistent with an increase in condensation reactivity when lipid is present.

Further evidence of strong lipid-framework interactions is given by the fitting of low-angle 1D XRD data for lamellar films of  $\text{SiO}_2$ , and BTESE templated with *diC*<sub>6</sub>PC to a lamellar model is illustrated in Figure 8.<sup>35</sup> Because of the (nonreflectivity) instrumental configuration used to collect this data, the data background is poorly simulated by this procedure. However, for determining the relative thicknesses of the lipid and inorganic layers in the lamellar structure the key parameter is the relative intensities of reflections, a feature in the scattering pattern that is well-reproduced by the simulated data. Our model for this lamellar structure (illustrated in Figure 8A) contains four variables: *L* and  $\sigma_L$ , the thickness and thickness variance of the lamellar unit cell, respectively, and *d*<sub>1</sub> and  $\sigma_1$ , the thickness and thickness variance of one phase in the unit cell, respectively. The assignment of this phase to the inorganic or organic layer is not possible from the data fit. However, it is still clear that extensive interpenetration (and thus interaction) is occurring between the lipid and silica phases in nanostructured *diC*<sub>6</sub>PC/ $\text{SiO}_2$ . While one *diC*<sub>6</sub>PC bilayer has a thickness of 25 Å, an *L* of 3.16 Å and a *d*<sub>1</sub> of 16.0 Å indicate that the thicknesses of both materials in each lamellae are equal, a structure that is only possible with near complete penetration of the phosphatidylcholine headgroup into the silica framework. For the *diC*<sub>6</sub>PC/BTESE data, *L* and *d*<sub>1</sub> (2.92 Å and 1.00 Å, respectively) indicate a minimum penetration of the lipid into the BTESE framework of only 0.6 Å (based on an assignment of *d*<sub>1</sub> to the BTESE phase). However, the large value of  $\sigma_1$  (0.7 Å) signifies the continued presence of significant interactions between lipid headgroups and the BTESE framework.

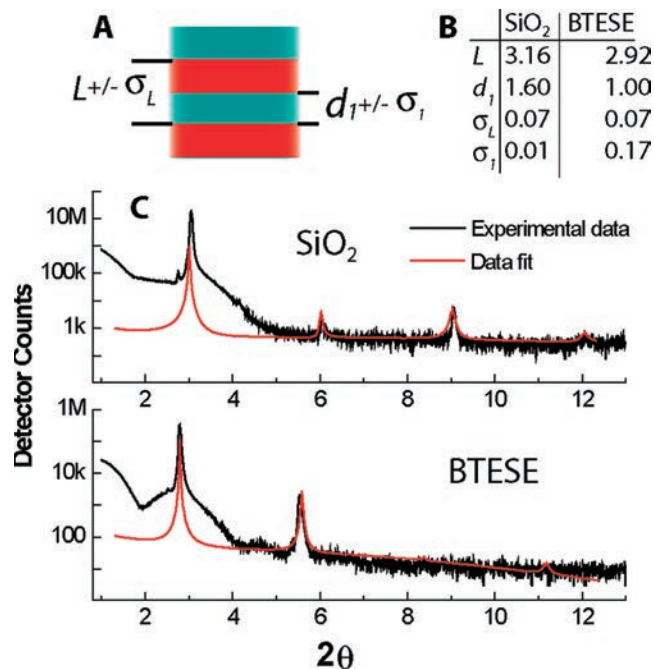


**Figure 8.** (A) Structural model used to fit 1D diffraction data for lamellar *diC*<sub>6</sub>PC/ $\text{SiO}_2$  and *diC*<sub>6</sub>PC/BTESE films, consisting of unit cell thickness *L* and thickness of phase 1 *d*<sub>1</sub>. (B) Fit parameters for this model obtained from the data in C. (C) Experimental and simulated data for lamellar *diC*<sub>6</sub>PC/ $\text{SiO}_2$  (top panel) and *diC*<sub>6</sub>PC/BTESE (bottom panel) films.

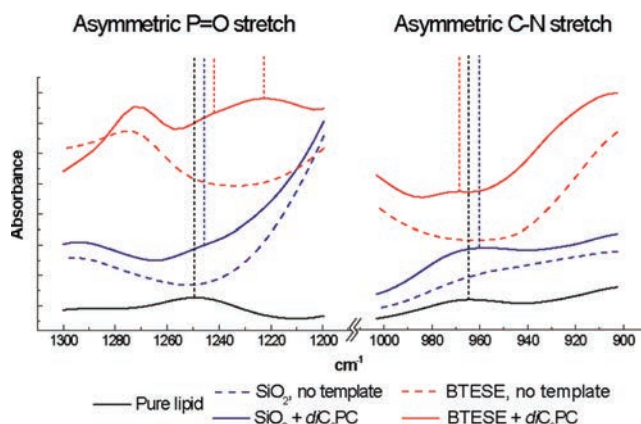


**Figure 9.** FTIR data for C–N and P=O stretches in *diC*<sub>6</sub>PC headgroup stretches in  $\text{SiO}_2$  and BTESE, as well as for pure lipid and nontemplated  $\text{SiO}_2$  and BTESE backgrounds.

To examine the chemical interactions between the lipid and framework phases, FTIR was used to probe the chemical environment of the phosphatidylcholine headgroup (Figure 9). Specifically, the vibrational regions for asymmetric C–N and P=O stretches were measured for *diC*<sub>6</sub>PC- and nontemplated  $\text{SiO}_2$  and BTESE as well as for pure lipid. The former vibration has been linked to dipolar interactions of the quaternary amine in the phosphatidylcholine headgroup,<sup>36</sup> while the frequency of the P=O band has been used as an indicator of hydrogen bonding in the phosphate group.<sup>36</sup> Both the *diC*<sub>6</sub>PC/ $\text{SiO}_2$  and *diC*<sub>6</sub>PC/BTESE materials show a shift in the P=O band to lower frequencies relative to that of the pure lipid, consistent with an increase in hydrogen bonding with the phosphate center (likely to free silanols at the interface between the lipid and framework

(34) Loy, D. A.; Carpenter, J. P.; Alam, T. M.; Shaltout, R.; Dorhout, P. K.; Greaves, J.; Small, J. H.; Shea, K. J. *J. Am. Chem. Soc.* **1999**, *121*, 5413–5425.

(35) Ruland, W.; Smarsly, B. *J. Appl. Crystallogr.* **2004**, *37*, 575–584.

(36) Popova, A. V.; Hinch, D. K. *Biophys. J.* **2003**, *85*, 1682–1690.

phases), with the BTESE-based material exhibiting more hydrogen bonding relative to that of silica. Also, this band is split into two peaks for *diC<sub>6</sub>PC*/BTESE films, suggesting the presence of more than one chemical environment. The C–N stretch can be interpreted as reflecting a more polar environment for the headgroup in the hybrid material relative to the material containing only silica in the framework.

As another means of examining the environment of the lipid headgroup, <sup>31</sup>P NMR chemical shifts for *diC<sub>6</sub>PC*/SiO<sub>2</sub> and *diC<sub>6</sub>PC*/BTESE materials were measured, yielding  $\delta = 5.3$  and 5.0 ppm, respectively. Although this small shift may be insignificant, the slightly larger chemical shift seen in the silica material could result from either small differences in the pH of the headgroup environment or by an increase in the relative negative charge on the *diC<sub>6</sub>PC* headgroup as a result of stronger hydrogen bonds. Again, FTIR proved to be a more sensitive probe for the comparison of chemical environment between the two types of templated material; future experiments should enable a better understanding of the discrepancies in material structure/chemical environment depicted by each analytical technique.

### Conclusions

We have characterized the nanostructure of silica- and hybrid-thin films synthesized using EISA with phospholipid templates and found that a variety of phases (1D, 2D, and 3D) can be formed by proper selection of the lipid structure. Also, lipid-framework interactions in these materials appear to be very

strong, with suppression or enhancement of siloxane framework reactivity. Other types of nanostructures (e.g., those based on bicontinuous minimal surfaces) may, in the future, be accessible using other biologically derived lipid types (for example, glycerates or bile salts) and will be explored in future research.

**Acknowledgment.** Use of the APS is supported by the Department of Energy under contract DE-AC02-06CH11357. Sandia is a multiprogram laboratory operated by Sandia Corporation, a Lockheed Martin Company, for the United States Department of Energy's National Nuclear Security Administration under contract DE-AC04-94AL85000. Partial support of this work (TMA) was through the DOE BES funding to Sandia, Sandia's Laboratory Directed Research and Development (LDRD) Programs, as well as through Air Force Office of Scientific Research Grant FA 9550-07-1-0054 and the National Institutes of Health through the HHH Roadmap for Medical Research Award number PHS 2 PN2 EY016570B. Images in this article were generated in the University of New Mexico Cancer Center Fluorescence Microscopy Facility, supported as detailed on the webpage <http://hsc.unm.edu/crtc/microscopy/Facility.html>.

**Supporting Information Available:** NMR characterization of the initial hydrolysis and condensation kinetics for TEOS solutions with *diC<sub>6</sub>PC*, CTAB, and no template. This material is available free of charge via the Internet at <http://pubs.acs.org>.